


Energy harvesting potential assessment and systematic design for energy-regenerative shock absorbers on railway freight wagons

Liwei Dong^{1,2} , Heli Zhang^{3,4}, Jie Yu^{1,5} and Guobiao Hu⁶

Abstract

A large amount of vibration energy is dissipated in the secondary suspension systems of railway freight wagons, which can be harvested as renewable power supplies to serve more smart devices for onboard applications. This paper explores the vibration energy harvesting potential of freight wagons and deals with the systematic design issues of energy-regenerative shock absorbers (ERSAs). By considering the ERSA force interaction and realistic track irregularity, a vehicle-track coupled model is established to predict a more accurate vibration response. The parameter sensibility analysis reveals that the operation speed, vehicle load, and track irregularity are the most critical factors that can significantly affect the power generation performance. In addition, vibration energy harvesting potential assessment is conducted on American, German, and Chinese track spectrums and several field-measured freight lines, indicating an average power potential ranging from 33 to 960 W per absorber with a full-loaded freight wagon running at 90 km/h. Finally, a systematic design approach for ERSAs is proposed based on the prior feasibility assessment, a hybrid Grey Wolf Optimization and Particle Swarm Optimization (GWO-PSO) algorithm, and the vehicle-ERSA coupled model. The digital twin of an ERSA has been established and validated by a series of experimental tests. Taking the average power as the objective and setting the suspension vibration velocity, maximum generator rotation velocity, and maximum ERSA force as constraints, the optimized ERSA exhibits an output power of 63 W and 20.22% shock absorption on the secondary suspension. Meanwhile, the GWO-PSO has demonstrated an enhanced exploration ability than the conventional GWO in dealing with the constrained optimization problem of the ERSA design.

Keywords

Energy harvesting power potential, systematic design, energy-regenerative shock absorber, freight wagon, digital twin

1. Introduction

Due to the energy crisis and the demand for sustainable development, energy efficiency and energy saving have drawn a worldwide concern in the transportation industry. Energy harvesting is an advanced and rapidly developing energy-saving technology that converts ambient potential renewable energy, such as vibration (Bakhtiary Yekta and Fakhari, 2023; Qin et al., 2023), wind (Dash et al., 2022), solar radiation (Aboelmaaref et al., 2021), and magnetic field (Kuang et al., 2021), into electricity. The railway system has many scenarios with large-scale vibration sources that can be harvested, otherwise dissipated (Jerrelind et al., 2021). More than energy reutilization, vibration energy harvesting technology aims to solve the distributed power supply problem of onboard devices, avoiding the inconvenience

caused by the cable installation of traditional power supply or regular replacement of chemical batteries.

¹Institute of Rail Transit, Tongji University, Shanghai, China

²School of Civil and Environmental Engineering, Nanyang Technological University, Singapore, Singapore

³College of Management Science, Chengdu University of Technology, Chengdu, China

⁴Institute of Operations Research and Analytics, National University of Singapore, Singapore, Singapore

⁵Zhuzhou CRRC Times Electric Co., Ltd., Zhuzhou, China

⁶Internet of Things Thrust, The Hong Kong University of Science and Technology (Guangzhou), Nansha, Guangzhou, Guangdong, China

Corresponding author:

Liwei Dong, Institute of Rail Transit, Tongji University, No.4800 Caoan Highway, Jiading District, Shanghai 201804, China.
Email: victor@tongji.edu.cn

Especially for unpowered railway freight wagons, access to economic power is urgently needed but limited (Dong et al., 2022). Facing the growing demand for self-powered applications in the railway industry, researchers have carried out long-term and in-depth research on high-performance energy harvesters.

The early generation of energy harvesters is small-scale for the onboard self-powered applications of wireless sensor nodes (WSNs). The power consumption of Zigbee WSNs is generally at the microwatt to milliwatt level (Gao et al., 2018). Although there is a low power demand, the researchers still try to enhance the power density enabling them to be lightweight. Being easy to install and having no influence on the original vehicle structures are their advantages. The three most common energy conversion mechanisms of small-scale energy harvesters are piezoelectric (Hegendörfer et al., 2023), electromagnetic (Delattre et al., 2023; Wu et al., 2021), and triboelectric (Hu et al., 2022; Jin et al., 2020). Dziadak et al. (2022) proposed a double-arm piezoelectric mounted on the freight wagon bogie for powering a WSN. It could generate a power of $73 \mu\text{W}$ at typical bogie vibration. Gao et al. (2020) developed an electromagnetic energy harvester driven by the inertial pendulum and ring gear-pinion transmission. In field tests, the harvester mounted on the bogie produced a stable voltage of 5 V and an average power of 250 mW with the DC/DC converter. Another pendulum-driven electromagnetic energy harvester with a mechanical motion rectifier (MMR) was reported by Fang et al. (2022). Du et al. (2021) proposed a multi-mode triboelectric energy harvester by combining contact-separation and floating sliding mechanisms to scavenge the mechanical energy of freight wagon couplers. The harvester charged a $470 \mu\text{F}$ capacitor to 5.2 V in 100 s at a 2.5 Hz excitation of 52 mm amplitude. To break through the power density of a single harvesting mechanism, Jin et al. (2017) proposed a triboelectric-electromagnetic hybrid energy harvester for self-powered train monitoring. The operations of triboelectric part and electromagnetic part are based on contact-separation mode and magnetic levitation motion respectively; correspondingly, peak power densities of 0.34 mW/g and 0.12 mW/g were achieved by them.

However, in order to meet the demand for higher power, large-scale energy harvesting technology has been studied and proposed. Large-scale energy harvesters convert and amplify vehicle vibration to rotation by mechanical mechanisms and then drive the electromagnetic generator to generate power. They are also called energy-regenerative shock absorbers (ERSAs). ERSAs are usually installed in the vehicle suspension system to convert and utilize the mechanical energy originally dissipated in the traditional shock absorbers. The commonly used motion conversion mechanisms are nut-screw (Wang et al., 2020) and rack-pinion (Li et al.,

2013), followed by the slider-crank (Li et al., 2021) and two-leg (Maravandi and Moallem, 2015) being proposed. Another essential part of an ERSA is the MMR which rectifies a bidirectional rotation to unidirectional rotation with several gears and one-way clutches. The concept of MMRs is proposed by referring to the working principle of rectifiers in the electronic field. Half-wave MMRs only transmit mechanical energy in one direction (Mi et al., 2020), and full-wave MMRs transmit that in both directions (Pan et al., 2019). In addition, it is demonstrated that the combination of an MMR and flywheel can increase the system inertia and improve the output voltage stability (Lin et al., 2018), making it easier to match with the power management circuit.

Since the current ERSA structure is compact and reliable enough, how much power can be harvested in a vehicle suspension system is widely concerned. Zhang et al. (2017) investigated the damping energy harvesting potential of automobile suspension systems with quarter suspension models. The harvestable power per absorber of a car, an off-road vehicle, and a bus at 60 km/h on class C road was predicted to be about 105, 384, and 1152 W, respectively. Abdelkareem et al. (2019) demonstrated that the potential power of a full-load truck suspension is about 71–434 W and 287–1733 W on class C and D roads. Wang et al. (2022) theoretically assessed the power potential of the primary and secondary suspensions of high-speed railway trains. The results showed that the ERSA could generate 5–30 W and 5–45 W when installed on the primary and secondary dampers, respectively.

Herein, a citespace research on hotspots of vibration energy harvesting was conducted based on recent literature, as shown in Figure 1. It is not difficult to find that hotspots are concentrated in terms of design, optimization, performance and electromagnetic. According to the applications of vibration energy harvesting in railway transportation, ERSAs have been deemed as a promising scheme for railway freight wagons to achieve self-power applications, thus reducing manual maintenance and enhancing train safety, as shown in Figure 2. As a kind of electromagnetic vibration energy harvester, ERSAs also need further attention from the perspective of optimization and design. The current research gap can be classified into the following two aspects: (1) Evaluation of the energy harvesting potential from railway freight wagons is lacking. Trends in heavy-duty and higher-speed freight railways will definitely accompany more intense vibrations and potential harvestable energy. In addition, the demand of unpowered wagons for some smart devices, such as electronically controlled pneumatic (ECP) braking systems, to improve vehicle performance is urgent but limited by the shortage of electrical cables. An energy harvesting potential prediction will assess in advance whether the current operating wagon and environment can offer

potential power can meet the device demand in self-powered applications. (3) An MMR-based ERSA is selected as the optimization object, and its digital twin is established by considering the engagement and disengagement modes of one-way clutches. The effectiveness of the digital twin is validated through experimental tests. (4) A novel systematic design approach for ERSAs is proposed to enhance output power based on the prior feasibility assessment, GWO-PSO algorithm, and vehicle-ERSA coupled model. Taking the suspension vibration velocity, generator rotation velocity, and maximum ERSA force as constraints ensures the reliability and practicality of the designed ERSAs. The GWO-PSO is proven to have a stronger exploration ability than a conventional GWO in dealing with the constrained optimization problem of ERSA.

This paper is organized as follows. Section 2 introduces the modeling of the vehicle-ERSA model. The parameter sensibility analysis and energy harvesting potential assessment are presented in Section 3. Section 4 establishes the digital twin of an MMR-based ERSA and proposes the systematic design approach. Section 5 validates the digital twin of the MMR-based ERSA with experiments and illustrates the optimization results. This paper is concluded in Section 6.

2. Mathematical modeling

2.1. The vehicle-track system

Vibration widely exists in railway vehicle-track systems and it is mainly caused by moving loads, track roughness, and parametric excitations. Moving loads induce flexural waves on the track and can be regarded as time-dependent action at fixed points. Track roughness refers to the random irregularity of the rail surface and

will cause forced excitations of the vehicle-track system. It will be discussed in detail in the next section. In addition, the stiffness of a wheel running on a discrete rail is variable. The harmonic components are determined by vehicle and track parameters. If the frequency matches the natural frequency of the vehicle, the excitation will be amplified and spread in the system.

The vehicle-track model is illustrated in Figure 3. The freight wagon can be divided into three components, namely, the carbody, the side frame, and the wheelset. The primary suspension is defined as the part connecting the wheelset and the side frame. In a freight wagon, rubber pads of the axle box are the main component of the primary suspension to provide primary stiffness and support function. The part connecting the side frame and the carbody is the secondary suspension system. The coil springs provide stiffness force, and the wedges provide damping force, converting the vibration into heat. ERSAs, as additional units, are usually installed parallel with coil springs, accounting for part of the damping effect and converting the absorbed vibration energy into electricity. ERSAs with different structures lead to different mechanical properties. However, the same thing is that they amplify the rotation velocity of the electromagnetic generator and its electrical damping with mechanical transmission. The amplified damping force accounts for an overwhelming proportion of the total force of ERSA; thereby, the ERSA is considered a damper in the energy harvesting potential assessment to make the analysis results more general and referential. The modeling of mechanical properties with more factors considered will be exploited in the optimization design process. The vertical force of the secondary suspension in front and rear bogies can be represented as

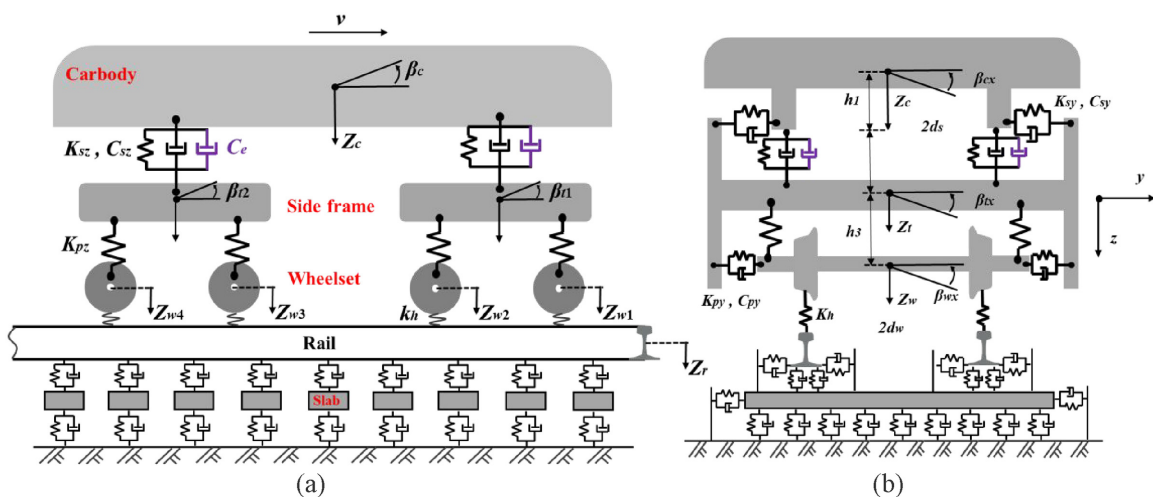
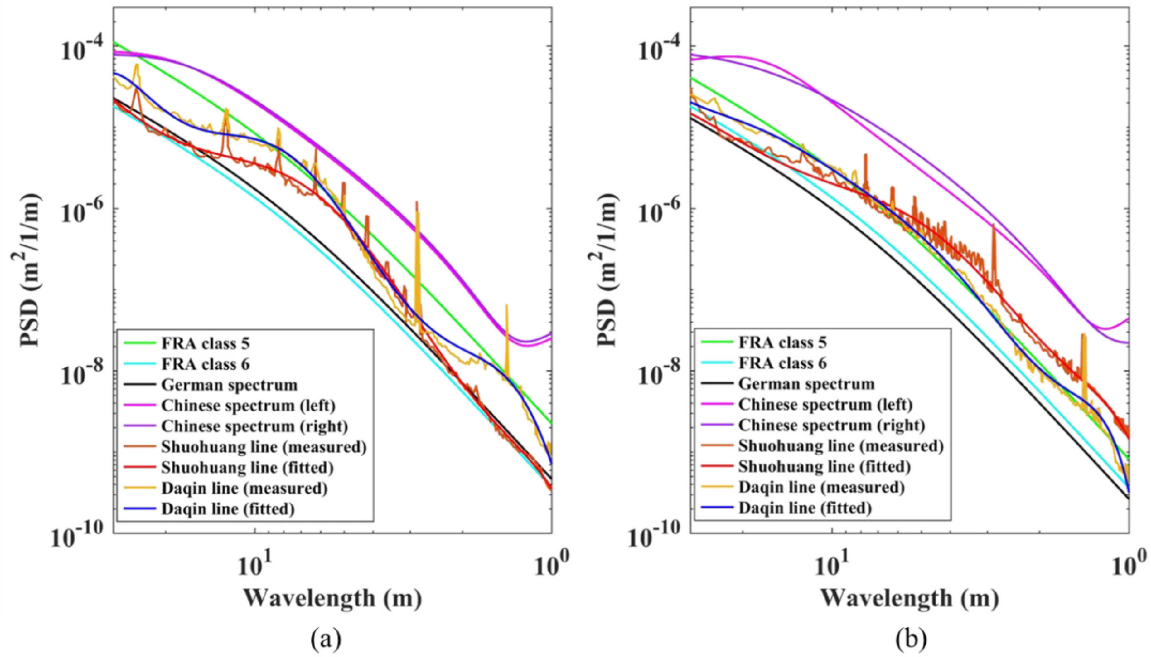


Figure 3. The vehicle-track dynamic model: (a) the side view of model and (b) the front view.

Table 1. Comparison of the track spectrum of freight lines in several countries.

	PSD of vertical irregularity	PSD of alignment irregularity	Max speed
FRA class 5/6	$S_v(\Omega) = \frac{kA_v\Omega_c^2}{\Omega^2(\Omega^2 + \Omega_c^2)}$	$S_v(\Omega) = \frac{kA_a\Omega_c^2}{\Omega^2(\Omega^2 + \Omega_c^2)}$	128/177 km/h
German high disturbance spectrum	$S_v(\Omega) = \frac{A_{v2}\Omega_{c2}^2}{(\Omega^2 + \Omega_{r2}^2)(\Omega^2 + \Omega_{c2}^2)}$	$S_v(\Omega) = \frac{A_{a2}\Omega_{c2}^2}{(\Omega^2 + \Omega_{r2}^2)(\Omega^2 + \Omega_{c2}^2)}$	250 km/h
Chinese speed-up main line spectrum	$S(f) = \frac{A(f^2 + Bf + C)}{f^4 + Df^3 + Ef^2 + Ff + G}$	$S(f) = \frac{A(f^2 + Bf + C)}{f^4 + Df^3 + Ef^2 + Ff + G}$	160 km/h

**Figure 4.** PSDs of several national standards and measured lines: (a) vertical irregularity and (b) alignment irregularity.

$$\begin{cases} F_{sfz} = K_{sz}[Z_c + l_1\beta_c - l_2\alpha_c - Z_{sf}] \\ \quad + C_e[\dot{\beta}_c + l_1\dot{\beta}_c - l_2\dot{\alpha}_c - \dot{Z}_{sf}] + (-1)^k 2\mu F_w \\ F_{srz} = K_{sz}[Z_c - l_1\beta_c + l_2\alpha_c - Z_{sr}] \\ \quad + C_e[\dot{\beta}_c - l_1\dot{\beta}_c + l_2\dot{\alpha}_c - \dot{Z}_{sr}] + (-1)^k 2\mu F_w \end{cases} \quad (1)$$

where K_{sz} represents the secondary suspension stiffness; Z_c is the carbody bouncing; l_1 is the half of the distance between wagon centers; β_c is the carbody pitching; l_2 represents the distance between secondary suspensions; α_c is the rolling of carbody; Z_{sf} and Z_{sr} are the bouncing of the front side frame and rear side frame, respectively; C_e is the equivalent damping of the ERSA; $k = 0$ or 1 indicates the unloading/loading case for wedges; μ and F_w are the friction coefficient and interaction force between the wedge and side frame.

The wheel-rail contact is a complex problem that has been studied extensively. It is considered as a rigid contact for simplification in this paper. The vehicle-track system is governed by:

$$[\mathbf{M}_s]\{\ddot{\mathbf{x}}\} + [\mathbf{C}_s]\{\dot{\mathbf{x}}\} + [\mathbf{K}_s]\{\mathbf{x}\} = \{\mathbf{f}_s\} \quad (2)$$

where \mathbf{M}_s , \mathbf{C}_s , \mathbf{K}_s represent the mass, damping and stiffness matrices; \mathbf{x} is the displacement vector; \mathbf{f}_s refers to the force vector.

2.2. Track irregularity

Track irregularity is introduced in evaluating the service state of railway tracks to ensure a safe and reliable operating environment for trains. It usually refers to the geometric deviation from the ideal position of the rails along longitudinal and alignment directions. Many countries, such as the United States, Germany, and China, have carried out extensive research and field tests to quantify track irregularity. Because track irregularity is one of the main reasons for inducing railway vehicle vibration, its precise description is necessary for vibration response calculation and energy harvesting potential assessment. Due to the randomness of track irregularity in the time domain, power

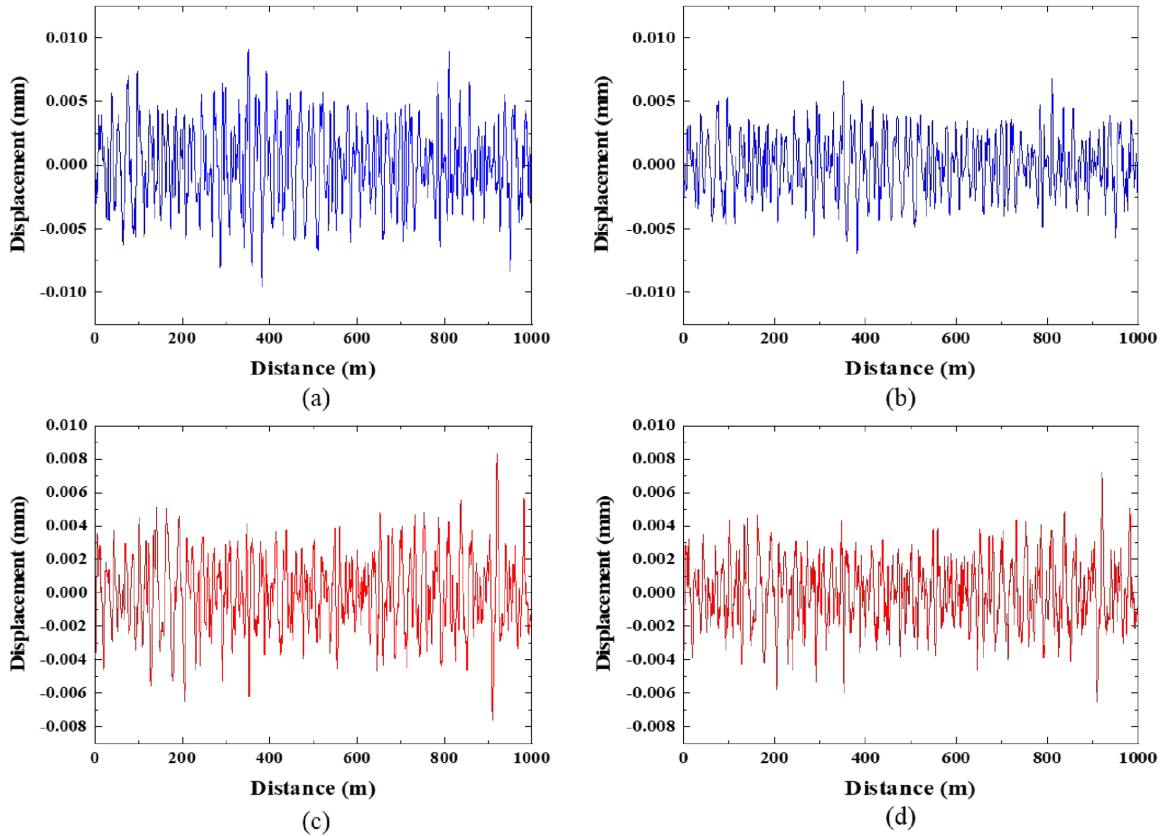


Figure 5. Track irregularity in the time domain based on fitted functions: (a) vertical irregularities of the Daqin, (b) Shuohuang lines, (c) alignment irregularities of the Daqin, and (d) Shuohuang lines.

spectral density (PSD) is exploited to describe the components at different wavelengths. The Federal Railroad Administration (FRA) of the United States classified track irregularity into nine classes, of which class 5 and class 6 are close to the actual road conditions of high-speed freight trains. Track irregularity in Germany is divided into high disturbance spectrum (for low speed) and low disturbance spectrum (for high speed), taking 250 km/h as the critical speed. Unlike the above two, the Chinese track spectrum and corresponding PSD function distinguish the left and right rails in vertical and horizontal irregularities (Zhai, 2015). For freight railway lines, the spectrum of the Chinese speed-up main line is usually exploited as model excitation for calculating the vibration responses of wagons. The comparison of the track spectrum of freight lines in several countries is presented in Table 1.

In Table 1, for the PSD of the FRA track spectrum, the safety factor k is usually chosen as 0.25; A_v and A_a are the track roughness constants for vertical and alignment directions; $\Omega = 2\pi f$ is the spatial frequency in the unit of $1/(\text{rad}/\text{m})$; Ω_c is the cut-off frequency. For the German high disturbance spectrum, A_{v2} and A_{a2} are the track roughness constants; Ω_{c2} and Ω_{r2} are the cut-off frequencies. For the Chinese speed-up main line spectrum, A , B , C , D , E , F , and G represent the characteristic parameters of PSD.

Daqin and Shuohuang lines are the two main freight lines in China. Their field-measured data are also added for comparison with other track spectrums with a wavelength of 1–30 mm, as shown in Figure 4. The detection of the Daqin line is under the condition of 555 km with an interval of 0.25 m, while the detection of the Shuohuang line is under 497 km with an interval of 0.25 m (Hao et al., 2023). The Chinese spectrum presents the most intense roughness for vertical irregularity, along with the FRA class 5. The irregularity level of the German high disturbance spectrum is slightly more intense than the FRA class 6. The levels of Daqin and Shuohuang lines are in between the two.

To simplify the calculation, the PSDs of Daqin and Shuohuang lines are fitted by polynomial functions and transformed into the data in the time domain for the model calculation, as shown in Figure 5.

$$\lg(s(f)) = \sum_{i=0}^8 a_i (\lg(f))^i + \dots + a_8 (\lg(f))^8 \quad (3)$$

In Figure 5, the vertical track irregularity of the Daqin line in the time domain is obviously more intense than that of the Shuohuang line, which is consistent with the fitted PSD function in Figure 2. Although the vehicle parameters and speed are the same, due to the difference of track irregularity, the vibration response and

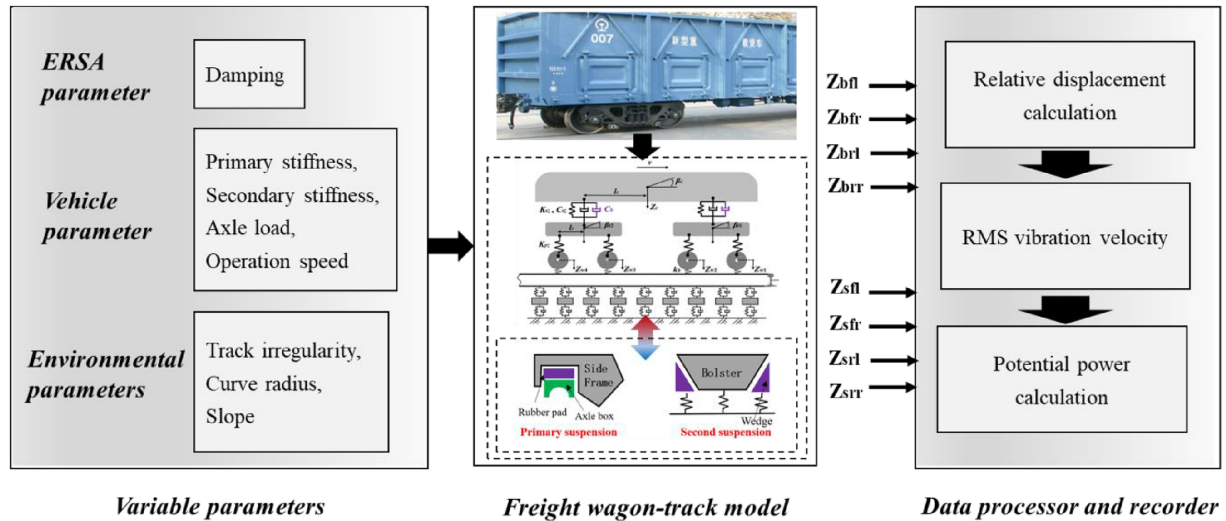


Figure 6. Research and analysis process of vibration energy harvesting potential assessment.

energy harvesting potential may be quite different. Hence, track irregularity is a crucial factor to consider in designing such energy harvesters.

2.3. Analysis process

The research and analysis process of this work is illustrated in Figure 6. The equivalent damping, as the most important parameter of ERSA, should be primarily considered in the energy harvesting potential assessment. In addition, the effects of the vehicle and environmental parameters on the power potential are also analyzed and discussed. The vibration responses of side frames and vehicles are calculated by the vehicle-track model, assuming that the four ERSAs are symmetrically installed on the secondary suspension of the front and rear bogies. Take the ERSA on the left side of the front bogie as an example, the average generated power without energy loss considered can be expressed as

$$P_{fl} = C_e \left(\frac{1}{n} \sum_{i=1}^n (\dot{Z}_{bfl} - \dot{Z}_{sfl})^2 \right) \quad (4)$$

where Z_{bfl} and Z_{sfl} are the vertical vibration displacements of the left side of the front carbody and the side frame.

In the following analysis, front and rear absorbers will be discussed respectively with data from the same side. K6 bogies, as a classic bogie type, have been exploited by nearly half of freight vehicles in China, thereby the vehicle type is selected as C80 wagon equipped with K6 bogie. Without special instructions, the simulated condition is that the vehicle with 90 t load runs on the railway line with the road roughness of FRA class 5 and without curves and slopes at 90 km/h.

3. Potential assessment

3.1. Effect of absorber damping

Due to the electrical damping, ERSAs not only convert vibration into electricity but also reduce vibration. As shown in Figure 7, the root mean square (RMS) vibration velocity decreases significantly with the damping increases from 0 to 250 kN·s/m. If the coupling between the ERSA and the vehicle-track model is not considered, the energy potential assessment will be seriously inconsistent with the actual situation. The RMS vibration of the front absorber is first slightly larger, then less than that of the rear absorber with the increase of damping, which is also reflected in power performance. Although the RMS vibration velocity decreases with the increase of damping, the average power always increases, but the growth tends to level off. The average power only increases by 10%, with the damping doubling from 1000 to 2000 kN·s/m. Excessive damping of ERSA cannot significantly improve the power but will make the manufacturing and implementation challenging. With the investigation of several railway vertical shock absorbers on secondary suspension, the damping value ranges from 25 to 217 kN·s/m (Zhai, 2015). The damping within 1000 kN·s/m is in the same order of magnitude as conventional railway shock absorbers, thereby it is feasible in terms of the production process and this range can be deemed a reasonable design region. Without special instructions, the damping value is 1000 kN·s/m in Sections 3.2, 3.4, and 3.6.

3.2. Effects of vehicle speed and track irregularity

According to the results in Section 3.1, the damping of 1000 kN·s/m is conducive to power generation. Hence, the damping is set to this value, and the vehicle load is

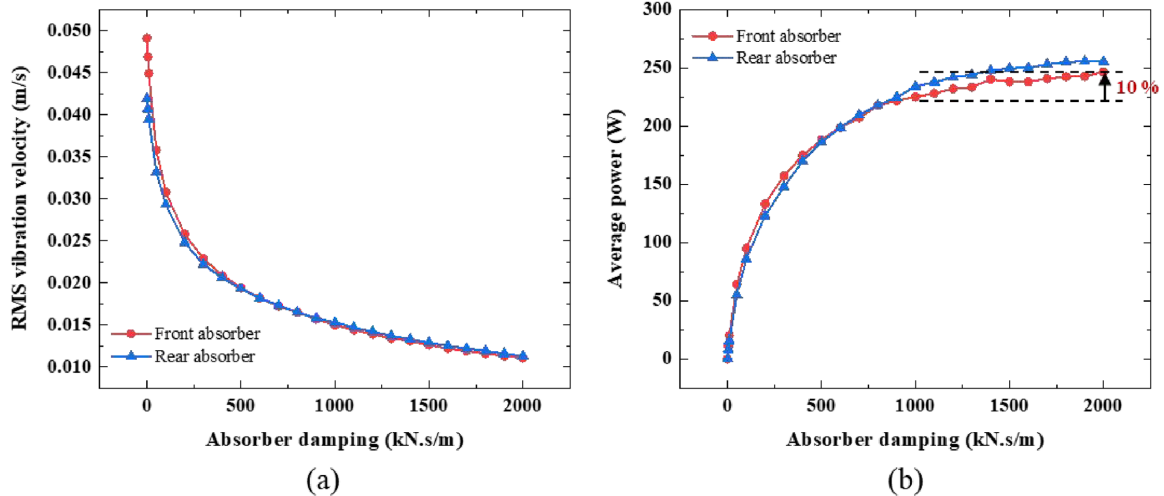


Figure 7. (a) RMS vibration velocity and (b) average power of absorber versus the damping.

90 t. The track irregularity class of FRA from high to low indicates the increase in road roughness. Due to the small difference in the calculation results of the front and rear shock absorbers, the RMS vibration velocity takes the average value of them in this section and Section 3.3. As shown in Figure 8, the RMS vibration velocity increases with the road roughness, offering greater potential for energy harvesting. In addition, a higher operation speed is also a favorable condition for power generation. The single ERSA can generate an average power of nearly 4000 W on the FRA class-1 road at 90 km/h, which indicates that rugged high-speed freight lines are an excellent application scenario to bring the greatest potential economic benefits by installing ERSAs. However, the two factors are also in conflict: the freight train has to slow down to ensure safety on the rugged line.

3.3. Effect of vehicle load

To improve transportation efficiency, heavy-duty freight trains with large vehicle loads are becoming trendy. Because the vehicle load is a vehicle parameter that affects the dynamic response of the vehicle interior, several groups of data with different ERSA damping are exploited for comparison. The vehicle speed is 90 km/h in the calculation process. As shown in Figure 9, the RMS vibration velocity and average power firstly increase with the vehicle load and then decrease. The most intense vibration occurs when the vehicle load is 60 t, which is because the natural frequency of the car body changes with the vehicle load and approaches the excitation frequency transmitted to the vehicle body. However, due to shock absorbers, the vibration generated by resonance is suppressed. The vibration suppression effect is most obvious when the vehicle load is 60 t, and is further enhanced with the increase of damping value.

3.4. Effect of road slope and curve

Uphill and downhill are often encountered on mountain roads in remote areas. In this section, the speed of the freight wagon is set to 60 km/h for safety operation. The vehicle nodding motion in the uphill and downhill processes will be affected, so the performance of the front and rear shock absorbers is analyzed. As shown in Figure 10, on the uphill, the RMS vibration velocity and average power of the front absorber increase with the slope, while those of the rear absorber first decrease, then increase. The vibration velocity gap is narrowed on a large slope. On the downhill, the RMS vibration velocity and average power of the front and rear absorbers increase with the slope, and there is no obvious change in the gap between them. From the average power of the front and rear absorbers, both uphill and downhill increase their power generation.

Another environmental parameter considered is the curve radius, as shown in Figure 10(b) and (c). A gentle curve with a radius over 3000 m hardly affects the wagon vibration. However, the RMS vibration velocity and average power reduce sharply at a sharp curve with a radius of less than 3000 m. The average power is only 40% of that on a straight line when the radius is 800 m.

3.5. Parameter sensitivity analysis

The potential power is normalized in the parameter sensitivity analysis, and the value here is the average of four absorbers. Herein, the initial damping is 500 kN/s/m, the speed is 50 km/h, the load is 50 t, the track irregularity is FRA 5, the curve radius is 3000 m, the primary stiffness is 170 MN/m, and the secondary stiffness is 3.75 MN/m. Additionally, the road slope ranges from -12 to 12 ‰ with an interval of 4 ‰. As shown in Figure 11, the power potential of the absorber strongly depends on the operation speed, vehicle load,

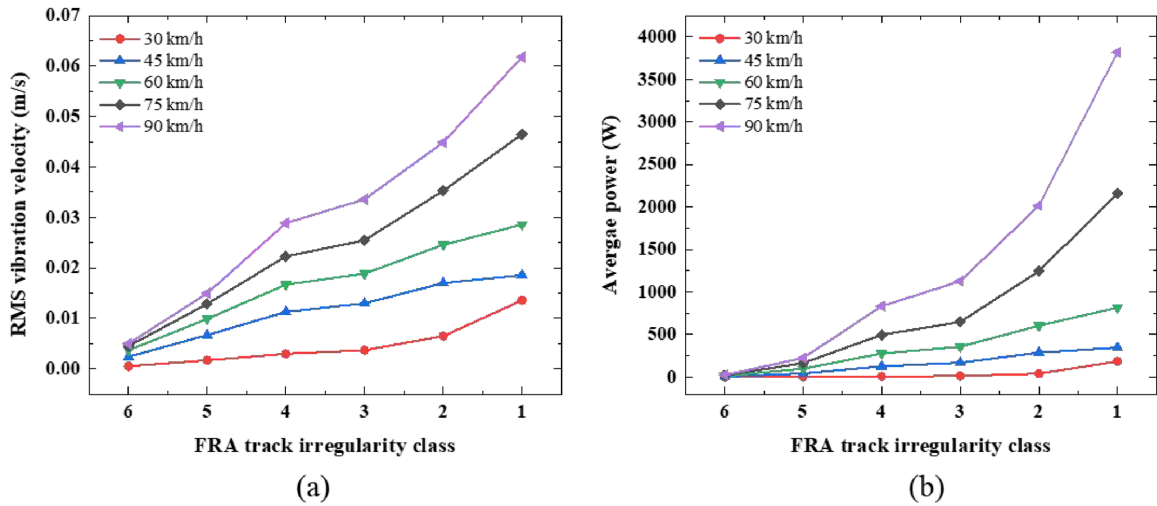


Figure 8. (a) RMS vibration velocity and (b) average power of absorber versus operation speed and track irregularity.

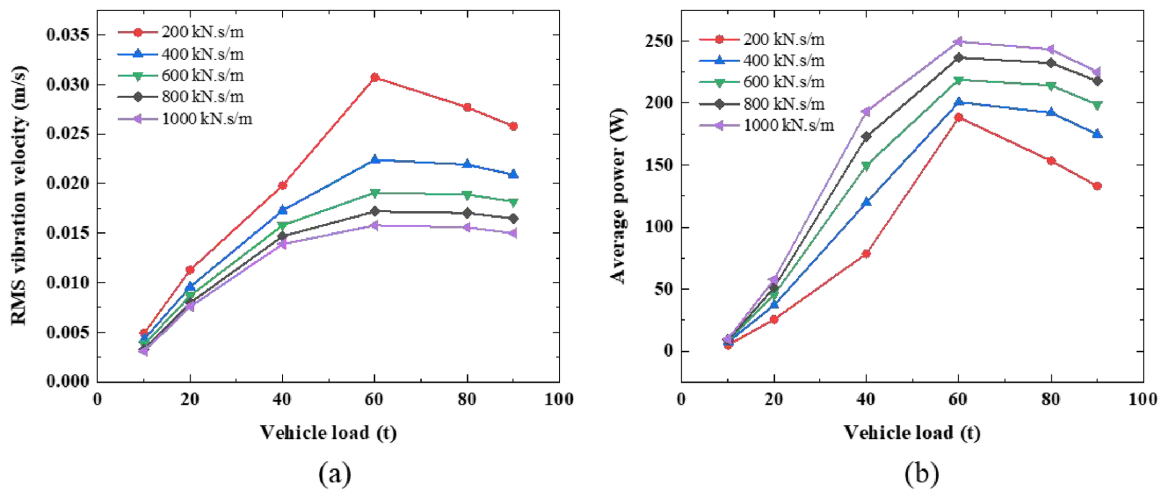


Figure 9. (a) RMS vibration velocity and (b) average power of the absorber versus the vehicle load.

and track irregularity. The increase in them leads to a bad driving condition and more intense vibrations, but a better condition for vibration energy harvesting. Secondly, slope and curve are two factors that have slight effects. Uphill and downhill are both beneficial for power generation, while a sharp curve will reduce vibration and power generation. In addition, the parameter sensitivity to the primary and secondary stiffness is also analyzed. However, the two parameters have no noticeable influences on the potential power. Meanwhile, their values are determined during the vehicle design process and cannot be arbitrarily changed in most situations.

3.6. Power potential prediction on several railway freight lines

Due to differences in regions and environments, many countries have developed their own track irregularity

PSDs based on abundant field tests. Here, several track spectrums for railway freight lines, including FRA class 5 and 6, German high disturbance spectrum, China speed-up main line spectrum, and measured spectrums of Shuohuang and Daqin lines (two most important freight transportation lines of China) are exploited to investigate the power potential of ERSAs in different situations. The ERSA damping is considered as 1000 kN.s/m to explore potential harvestable vibration energy. Figure 12 presents the time-history vibration velocity and absorber power on the Shuohuang line. The vibration intensity and generated power increase obviously with speeding up. It is noted that the ratio of peak vibration velocity to its RMS value is about 3, which reflects a more noticeable variation in output power. Such a long-span of them is a challenge to the design of ERSAs and charging circuits.

The average power outputs per absorber on several railway freight lines are plotted in Figure 13, and the

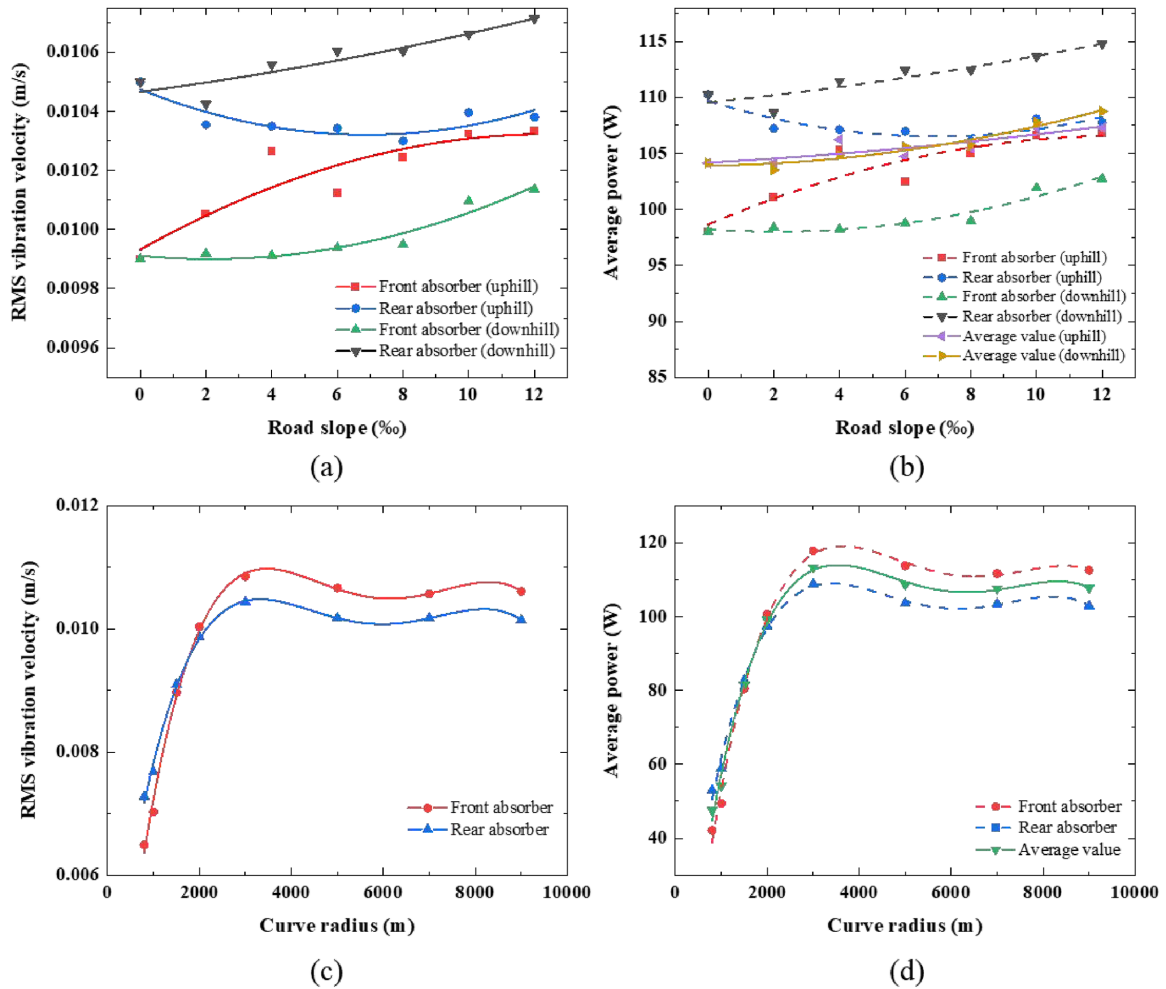


Figure 10. (a) RMS vibration velocity, (b) average power of the absorber versus the road slope, (c) RMS vibration velocity, and (d) average power of the absorber versus the curve radius.

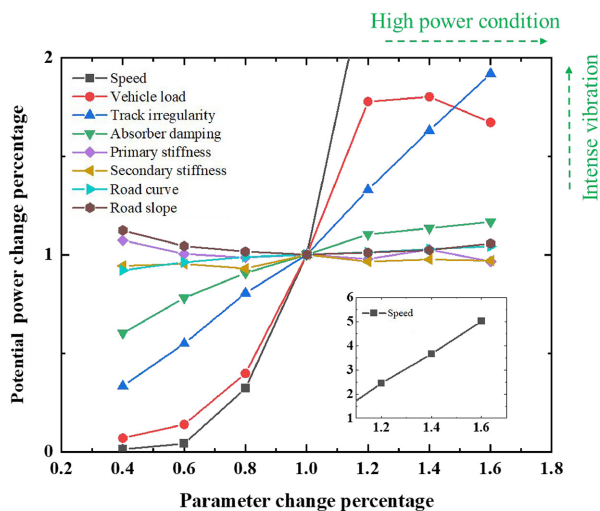


Figure 11. Parameters sensitivity analysis of the energy harvesting performance.

detailed data are listed in Table 2. The performance on the Chinese spectrum is the best, with an average power

of 153–961 W per absorber with the vehicle speed ranging from 30 to 90 km/h, followed by FRA class 5, which is because the Chinese spectrum reflects a greater unevenness of the railway track than that of other countries. The performance on the Daqin line has superiority compared with that on the Shuohuang line, and they are in between FRA class 5 and class 6. A good performance reflects the poor condition of roads, mostly early railway lines or in remote areas. An economic power supply is very significant in helping improve vehicle performance and provide reliable monitoring.

4. Systematic design approach

4.1. Digital twin of an MMR-based ERSA

A type of mechanical ERSA is exemplified as illustrated in Figure 14. The ERSA mounted on the secondary suspension by the rings at both ends converts the vertical vibration into electricity. It is composed of a mechanical transmission part and an electromagnetic generator.

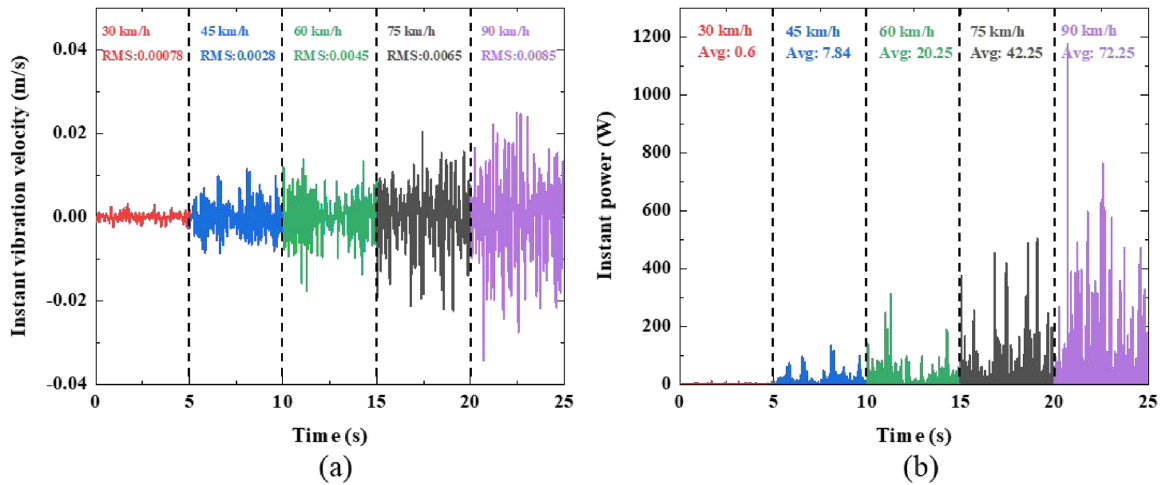


Figure 12. (a) Time-history vibration velocity and (b) the absorber power on the Shuohuang line.

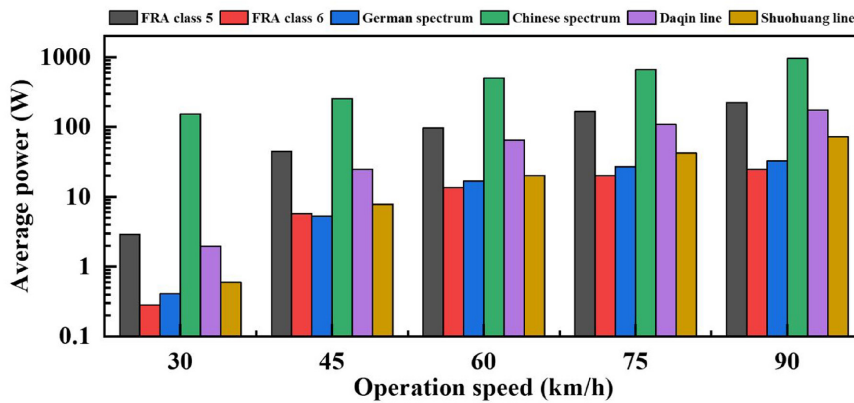


Figure 13. Average power potential prediction on several railway freight lines.

Table 2. Power potential prediction of a 90 t loaded freight wagon at 90 km/h on several freight lines.

	30 km/h	45 km/h	60 km/h	75 km/h	90 km/h
FRA class 5	2.89 W	44.89 W	98.01 W	166.41 W	225 W
FRA class 6	0.28 W	5.76 W	13.69 W	20.25 W	25 W
German spectrum	0.41 W	5.29 W	16.81 W	27.04 W	32.49 W
Chinese spectrum	153.76 W	256 W	506.25 W	665.64 W	961 W
Daqin line	1.96 W	25 W	65.05 W	109.6 W	176.02 W
Shuohuang line	0.68 W	7.84 W	22.63 W	43.57 W	73.97 W

In the mechanical transmission part, the nut-screw pair converts the reciprocating vibration of the secondary suspension into bidirectional rotation. Then, the combination of three bevel gears and 2 one-way clutches, also called a mechanical motion rectifier, regulates the bidirectional rotation into unidirectional rotation. The upper one-way clutch is engaged in upward vibration, and the lower one-way clutch is engaged in downward vibration. Hence, we can ensure the rotation direction of three bevel gears and generator unidirectional. After

the velocity amplification, the electromagnetic generator rotates at a higher speed to generate considerable electricity. When the rotation velocity transmitted by the lead screw to the right bevel gear is less than its current velocity, both one-way clutches are disengaged, and the generator rotates with the inertia of its own and flywheel. The flywheel can improve the output voltage stability under stochastic vehicle vibration by storing the kinetic energy in the engagement mode and slowly releasing it in the disengagement mode.

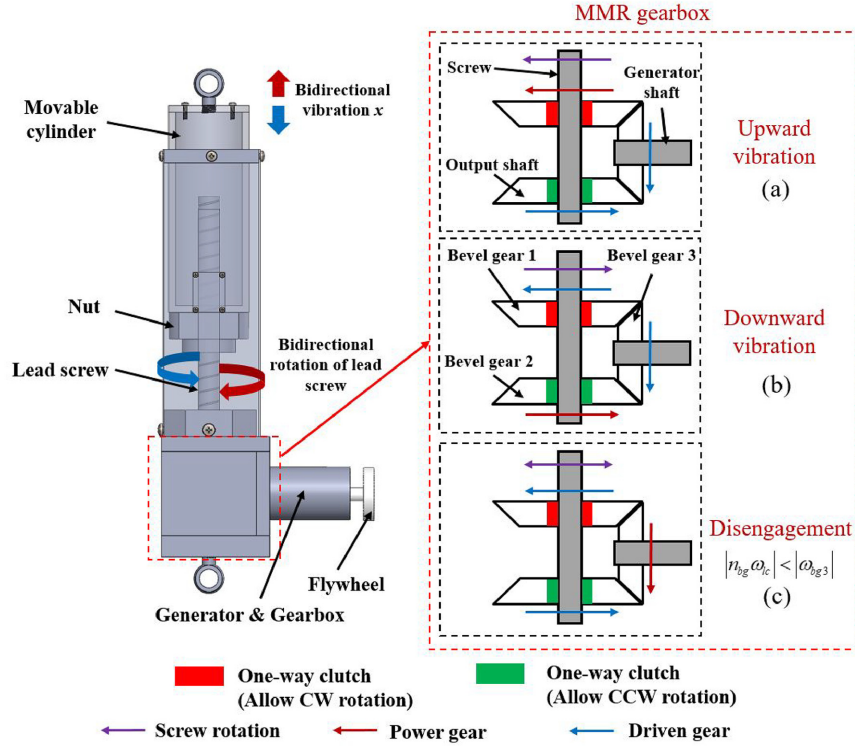


Figure 14. Configuration and working principle of a type of ERSA based on the nut-screw and mechanical motion rectifier.

The electromagnetic torque induced by the generator damping coefficient can be expressed as

$$\begin{cases} T_{ge} = C_{ge}\omega_{ge} \\ C_{ge} = \frac{3k_t k_e}{2(R_i + R_e)} \end{cases} \quad (5)$$

where ω_{ge} is the rotation velocity of the generator; k_e , k_t represent the voltage and torque constants of the generator; R_0 and R_e are the internal and external resistances of the generator.

The motion equation of the electromagnetic generator can be expressed as

$$T_m = \frac{3k_t k_e}{2(R_i + R_e)}\omega_{ge} + (J_{ge} + J_{fw})\dot{\omega}_{ge} \quad (6)$$

where J_{ge} and J_{fw} represent the inertia of the generator and the flywheel, respectively.

With the amplification of mechanical transmission, the rotation velocity of the generator can be obtained as

$$\begin{cases} \omega_{ge} = \frac{2\pi n_t}{l}\dot{z} \\ n_t = n_{bg}n_{pg} \end{cases} \quad (7)$$

where l is the lead of the screw; n_t is the total transmission ratio, which is determined by the transmission ratios of the bevel gear n_{bg} and planetary gearbox n_{pg} together.

The equivalent damping of ERSA can be obtained according to power conservation

$$C_e = \frac{T_{ge}\omega_{ge}}{\dot{z}^2} = \frac{6k_t k_e (\pi n_t)^2}{l^2(R_i + R_e)} \quad (8)$$

Based on the energy conservation, the kinetic energy of the system can be obtained related to the square of vibration acceleration, thereby deriving the equivalent inertia mass of the ERSA.

$$\begin{cases} E_k = \frac{1}{2}m_{nut}\dot{z}^2 + \frac{1}{2}\sum J_t\omega_{ts}^2 + \frac{1}{2}(J_{ge} + J_f)\omega_{ge}^2 = \frac{1}{2}M_e\dot{z}^2 \\ M_e = m_{nut} + \frac{4\pi^2}{l^2}\sum J_t + \frac{4\pi^2}{l^2}n_t^2 J_s \end{cases} \quad (9)$$

where m_{nut} is the mass of the nut; $\sum J_t$ is the total inertia of the mechanical components, including the screw and bevel gears. In most situations, $\frac{4\pi^2}{l^2}n_t^2 J_s \gg m_{nut} + \frac{4\pi^2}{l^2}\sum J_t$ due to the amplification of the total transmission ratio, and J_s is the total inertia of the generator and flywheel. To simplify the calculation of the equivalent inertia mass, it is possible to consider only the third term induced by J_s .

In the engagement mode, the force of the ERSA is compromised by damping force and inertia force, which is approximately equal to 0 in the disengagement mode since there is no power input for the ERSA.

$$\begin{cases} F_e = \frac{6k_t k_e (\pi n_t)^2}{l^2 (R_i + R_e) \eta_m} \dot{z} + \left[\frac{m_{nut}}{\eta_m} + \frac{4\pi^2}{l^2 \eta_m} \sum J_i + \frac{4\pi^2}{l^2 \eta_m} n_t^2 (J_{ge} + J_f) \right] \dot{z}^2 \\ F_e \approx 0 \end{cases} \quad \begin{aligned} & \text{Engaged: } |n_{bg} \omega_{lc}| \geq |\omega_{bg3}| \\ & \text{Disengaged: } |n_{bg} \omega_{lc}| < |\omega_{bg3}| \end{aligned} \quad (10)$$

where η_m is the mechanical efficiency.

The phase open circuit voltage of the generator can be expressed as

$$\begin{cases} E_{gei} = k_e \omega_{ge} \sin\left(\theta + \frac{2i}{3} \pi\right), i = 1, 2, 3 \\ \theta = \int_0^t p \omega_{ge} dt \end{cases} \quad (11)$$

where i indicates the i th phase; θ is the electrical angle; p is the number of polar pairs. In the disengagement mode, the generator rotates on the inertia of its own and flywheel, and the rotation velocity can be expressed as

$$\omega_{ge} = \omega_{s0} e^{-\frac{C_e}{M_e}(t-t_0)} \quad (12)$$

where ω_{s0} and t_0 are the initial rotation velocity and initial time of the disengagement mode.

Hence, the phase open circuit voltage of the ERSA in both modes can be summarized as

$$\begin{cases} E_{gei} = \frac{2\pi k_e \dot{z}}{l} \sin\left(\int_0^t \omega_e dt + \frac{2k}{3} \pi\right) \\ \text{Engaged: } |n_{bg} \omega_{lc}| \geq |\omega_{bg3}| \\ E_{gei} = k_e \omega_{s0} e^{-\frac{C_e}{M_e}(t-t_0)} \sin\left(\int_0^t \omega_e dt + \frac{2k}{3} \pi\right) \\ \text{Disengaged: } |n_{bg} \omega_{lc}| < |\omega_{bg3}| \end{cases} \quad (13)$$

The generated power and efficiency of ERSA can be expressed as

$$P_{ge} = \sum_{i=1}^3 \frac{E_{gei}^2 R_e}{(R_i + R_e)^2} \quad (14)$$

$$\eta = \frac{\text{Avg}(P_{ge})}{\text{Avg}(P_{in})} \quad (15)$$

The digital twin of ERSA can be expressed as

$$\chi = \text{ERSA}(l, n_t, J_s, k_e, k_t, R_i, R_e) \quad (16)$$

where χ indicates the calculation results, including the rotation velocity of the generator ω_{ge} , ERSA force F_e , ERSA power P_{ge} , and ERSA efficiency η . The digital twin of ERSA is related to parameters, including the lead of the screw l , the total transmission ratio n_t , the total inertia of the flywheel and generator J_s , the generator voltage constant k_e , the generator torque constant k_t , the generator internal resistance R_i and the external resistance R_e .

4.2. Hybrid GWO-PSO algorithm

The hybrid GWO-PSO. Combines the advantages of both algorithms and can enhance global search ability and convergence speed (Shaheen et al., 2021). The basic principles of PSO and GWO have been provided in Appendix A. The process of GWO-PSO is executed as follows:

- (1) Random generation of the search agents and determination of the solution region;
- (2) GWO calculates the position of each wolf;
- (3) Update the position of each wolf according to the principle of PSO;
- (4) Update the parameters in GWO and calculate the fitness of each wolf;
- (5) Update the positions of alpha, beta, and delta wolves;
- (6) Repeat steps (2) to (5) before reaching the maximum number of iterations, or save the final optimal position and fitness.

4.3. Optimal design for ERSAs

4.3.1. Significance of power potential assessment and prior feasibility assessment. Section 3 has conducted the parameter sensitivity analysis and power potential assessment, which is helpful to accelerate the optimal design for ERSAs from the following two aspects:

- (1) The parameter sensitivity analysis indicates that the operation speed, vehicle load, and track irregularity are the main factors affecting the power generation performance, and the other parameters such as curve and slope have little effect on energy harvesting. Therefore, during the optimal design, in addition to the parameters of vehicles and railway tracks, we only need to clarify the operation speed, vehicle load, and track irregularity, thereby some unnecessary initial inputs (curve radius and slope) can be omitted and simplify the calculation process.
- (2) In Table 2, we have summarized the potential harvestable vibration power of freight wagons under different track spectrums and speeds. At the beginning of the design, our program will conduct a prior feasibility assessment by pre-estimating the maximum potential power with vehicle speed and track spectrum according to Table 2. If the power demand of ERSA is higher than the maximum potential power, which means there is no optimization solution. The optimization program will be directly

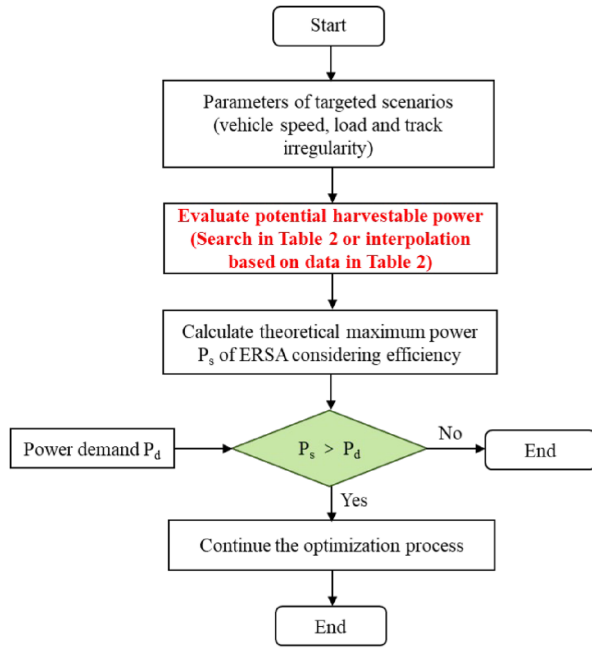


Figure 15. Logic of prior feasibility assessment.

Table 3. Typical power consumption of devices for freight wagons.

Devices	Quantity	Power consumption
ECP		
Onboard device of the ECP braking system	1	24 W
Wireless sensor node		
Communication module	1	320 mW
Computing module	1	40 mW
Axle temperature sensor	8	7.5 mW
Smoke detector	1	0.9 W

terminated to avoid long-time ineffective optimization. The logic of prior feasibility assessment is shown in Figure 15.

Herein, an example of the prior feasibility assessment is provided for better understanding. As shown in Table 3, If the wagon is equipped with an electronically controlled pneumatic (ECP) braking system (an advanced braking system with faster signal transmission) and wireless sensor node, the required minimum power supply is about 30 W. Assuming that the wagon with a 90 t vehicle load runs at 90 km/h on Daqin Line. Considering the average efficiency of ERSAs is about 40% here (Li et al., 2021), the theoretical maximum power in this situation is 70.04 W, which indicates that it is feasible to achieve an ERSA power of 30 W. Similarly, it is impossible to meet the power demand by using a single ERSA on FRA class 6, German spectrum, and Shuohuang line. Hence,

estimating the power potential in advance according to vehicle parameters and line conditions can evaluate whether the power demand can be met.

4.3.2. Downsizing of search space. In order to accelerate the optimization process, it is necessary to reduce the search space. The digital twin of ERSA is modeled with $l, n_t, J_s, k_e, k_t, R_i, R_e$. The lead of screw l determines the velocity amplification factor n_{sn} of the nut-screw mechanism. It can be determined in advance and adjusted with the total amplification factor of ERSA $n_{sn}n_t$ unchanged; thereby, it is preselected as 0.03 in this study. k_e, k_t and R_i are coupled generator parameters. If they are optimized simultaneously, the electromagnetic generator needs to be customized. Since the generator is usually chosen from off-the-shelf products to reduce manufacturing cost, k_e, k_t , and R_i are not considered in the optimization process. Therefore, the total transmission ratio of gears n_t , total inertia of generator and flywheel J_s , and external resistance R_e , which all directly influence the mechanical and electrical properties of the ERSA as well as the interaction with the vehicle, will be the essential design parameters in the optimization.

4.3.3. Problem formulation. The optimization of ERSA is implemented based on the vehicle-ERSA coupled model. The coupled model incorporates the vehicle-track dynamic model in Section 2.1 and the digital twin of ERSA in Section 4.1. The coupling between them has been considered due to non-negligible mutual mechanical interaction. The basic parameters of vehicle and track, as well as the operation speed, vehicle load, and track irregularity are determined according to the targeted scenario. They are the inputs of optimization model. The ERSA parameters to be optimized are the total transmission ratio of gears n_t , total inertia of generator and flywheel J_s , and external resistance R_e . The main aim of the optimization design is to meet the power needs of onboard devices. Thereby, maximizing the output power of the ERSA is the design objective. Meanwhile, the following design constraints have to be considered:

- (1) Although freight wagons have no special requirements for vehicle vibration and comfort, the vibration intensity of wagons equipped with ERSAs should preferably not exceed that of the original ones.
- (2) The maximum rotation velocity of the electromagnetic generator is not allowed to exceed the nominal rotation velocity, avoiding reduced service life and mechanical damage.
- (3) The maximum force of the ERSA is limited according to the practical requirements to ensure that the load of the mechanical mechanism is not excessive.

Hence, the constrained optimization problem of ERSA can be expressed as

$$\begin{cases} \min -P_{avg}(n_t, R_e, J_s) \\ s.t. g_1 = v_{rms} - v_s \leq 0 \\ g_2 = \omega_{gmax} - \omega_s \leq 0 \\ g_3 = F_{max} - F_s \leq 0 \end{cases} \quad (17)$$

where P_{avg} is the average power over the running time of the vehicle; v_{rms} and v_s are the RMS values of the secondary suspension vibration under the condition of the wagon with/without the ERSA; ω_{gmax} and ω_s represent the maximum velocities of the generator and the nominal rotation velocity of the generator, respectively; F_{max} and F_s are the maximum absolute value of the ERSA force and the designed maximum force of the ERSA.

4.3.4. Systematic design process. The process of the proposed systematic design approach is illustrated in Figure 16. It can be divided into the following steps:

- (1) Prior feasibility assessment on power demand and energy harvesting potential in the targeted application scenario, in which the vehicle speed, vehicle load, and track irregularity must be definite because they are the three most important factors affecting the energy harvesting potential. An example feasibility assessment has been presented in Section 4.3.1. It can avoid invalid optimization design due to the prediction of feasible solutions in advance.
- (2) Selection of the electromagnetic generator. The generator parameters, including the power, torque, rotation velocity, and internal resistance, should be carefully considered. If there is no suitable solution in the optimization based on the selected generator, the generator can be replaced again.
- (3) Parameter setting for the GWO-PSO and random generation of the initial population.
- (4) Interaction with the vehicle-ERSA model. The GWO-PSO generates or updates the design parameters (n_t , R_e , and J_s) and transmits them into the vehicle-ERSA model. It is noted that the force coupling between the vehicle and ERSA is considered in the model for a more accurate vibration response calculation and a more realistic application environment simulation. The generator velocity, ERSA force, power, and efficiency will be calculated for the next step.

- (5) Retrieving the global optimum position and fitness based on the updating principle of the GWO-PSO.

5. Optimization results and discussion

5.1 Experimental validation for the digital twin of ERSA

The experimental validation was carried out on a horizontal test bench, as shown in Figure 17. The test bench is driven by a stepper motor. The arbitrary rotation of the stepper motor is controlled by a signal generator and then converted into the repetitive linear motion of the slider with the nut-screw mechanism. An L-shape clasper fastened on the slider keeps the same motion and acts it the movable end of the ERSA. During the experiment, the vibration excitation, generator velocity, ERSA force, and ERSA phase voltage were measured and acquired by sensors and data acquisition devices to validate the ERSA digital twin.

Figure 18 compares the experimental and simulation results of the ERSA with an external resistance of 16 Ω at a periodic vibration excitation of 0.65 Hz and ± 7 mm amplitude. The force curve for one cycle corresponds to the rotation velocity and voltage curves for two cycles, which implies that the vibration energy in both directions is fully utilized. In the disengagement mode, the ERSA force was close to 0; the generator velocity was not immediately reduced to 0 but slowly descended with the inertial. The force sharply increased when it was switched to the engagement mode. The simulation voltage within the green box was larger than the experimental result. This is because the measured displacement input to the digital twin was impacted each time the force direction changed, resulting in some invalid displacement components measured. The test and simulation results show a good consistency. A series of tests were conducted to validate the effectiveness of the digital twin of ERSA, and the errors between the simulation and test data are illustrated in Figure 19. The amplitude of vibration excitation is ± 7 mm, and the frequency increases from 0.35 to 0.8 Hz with an interval of 0.15 Hz. Two sets of experimental data were used for comparison to avoid accidental experimental errors. The errors between simulation and test data in RMS values of the generator velocity, ERSA force, and ERSA voltage range from 2.54 to 4.54%, 8.25 to 15.78%, and -4.28 to 8.12%, respectively. The overall errors are acceptable, which indicates the digital twin of ERSA can be used for optimization design.

5.2 Optimization results

5.2.1. Fitness, constraint function values, and optimized parameters. In this section, the optimization is executed

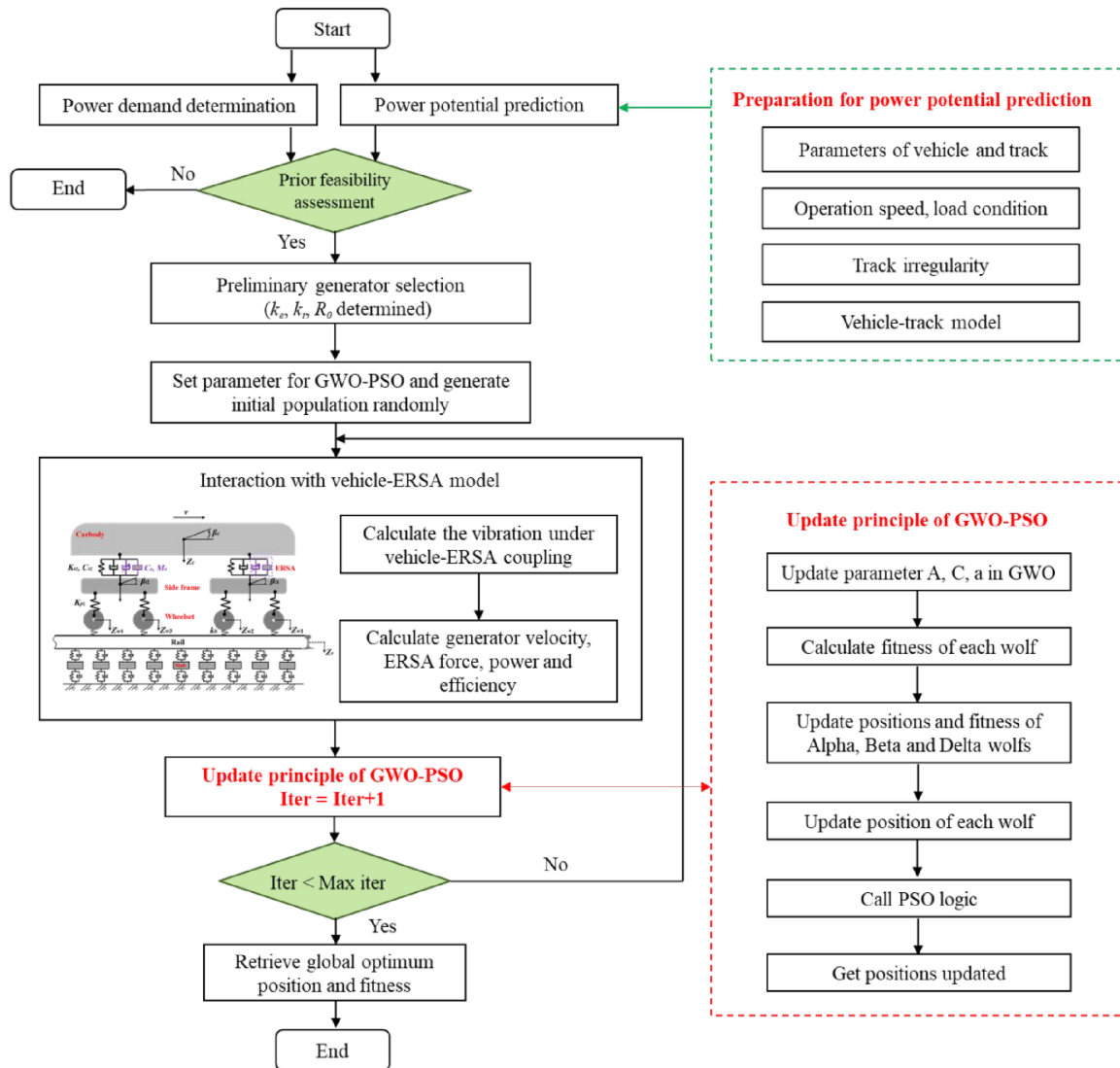


Figure 16. Systematic design process for ERSAs.

under the situation where the freight wagon runs at 90 km/h on the Daqin line. The aim is to harvest an average power over 30 W to meet the power demand of devices listed in Table 3. The prior feasibility assessment in Section 4.3.1 implies that there are potentially feasible solutions to meet the design requirements. Thereby, the optimization is conducted by following the procedures in Figure 16 and optimization objective equation (17). The nominal rotation velocity ω_s is 938 rad/s, and the F_s is the designed maximum force for the ERSA. The parameters of the selected generator are listed in Table 4.

Figure 20 illustrates the variation of values of the fitness function in the iteration process. The GWO and GWO-PSO with the same parameter settings are applied to deal with the same optimization problem for comparison. The GWO was trapped in a local optimum at the 25th iteration, while the GWO-PSO found a better solution at the 73rd iteration, obtaining an

average power of 63 W. Figure 21(a) to (c) present the variation of values of the constraint functions g_1 , g_2 and g_3 . g_1 obtained by GWO-PSO is lower than that obtained by GWO in the iteration, which demonstrates that the ERSA optimized by the GWO-PSO has a better shock absorption ability. g_2 and g_3 obtained by the GWO-PSO are finally closer to 0, which implies the maximum generator rotation velocity and the ERSA force approach their corresponding constraint values. During the optimization process with the GWO, only g_3 is close to 0, while g_2 is still very small, leading to an unsatisfactory result. The optimized parameters of n_t , R_e and J_s are 32, 2.34 Ω , 0.1 kg/m³, respectively. Overall, the GWO-PSO exhibits a better exploration ability than the GWO in dealing with the constrained optimization problem of the ERSA design.

Generally, the output three-phase voltage of the generator needs to be regulated by a rectifier and a DC/DC converter and finally be stored in a battery or

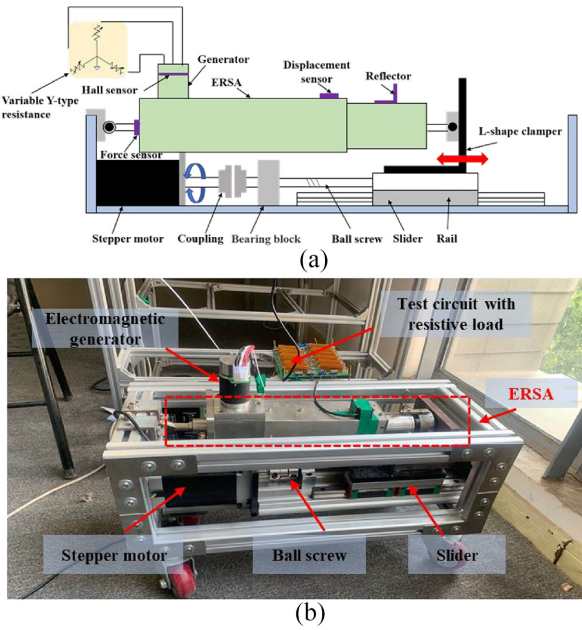


Figure 17. Horizontal test bench and experimental setup.

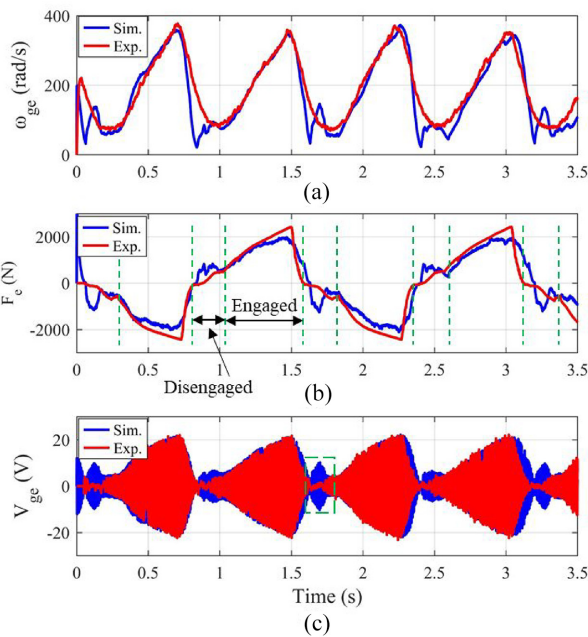


Figure 18. Comparison between simulation and test results of the ERSA: (a) generator rotation velocity, (b) ERSA force, and (c) the generated phase voltage of ERSA.

supercapacitor. In the above design, the optimized external resistance is constant, which can be implemented by the DC/DC converter using the fractional open-circuit voltage (FOCV) technology (Dong et al., 2023). The FOCV controls the input voltage of the DC/DC converter to a constant scale of the open-circuit voltage, which can implement an approximately constant equivalent resistance of the circuit. The voltage scale factor in the FOCV should be set according to the

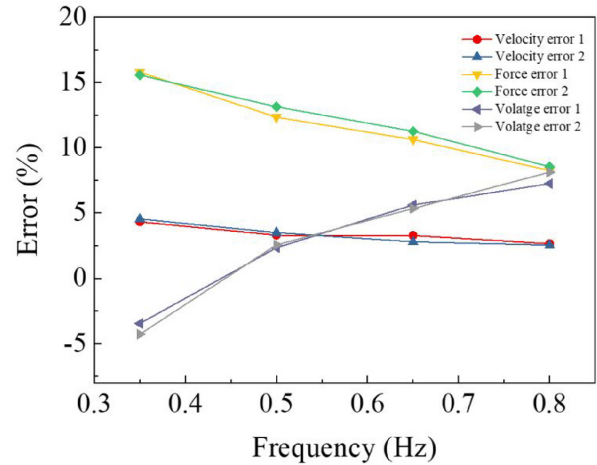


Figure 19. Errors between simulation and test data in several conditions (1/2 indicate the errors with first/second test results).

Table 4. Parameters of selected generator.

Symbol	Value	Description
k_e	0.0445 V/rad	Voltage constant of the generator
k_t	0.0445 N·m/A	Torque constant of the generator
R_i	1.29 Ω	Internal resistance
L_i	0.395 mH	Internal inductance
U_e	48 V	Nominal voltage
I_p	37.2 A	Maximum peak current
ω_e	938 rad/s	Nominal rotation velocity

Table 5. Comparison of ERSA designed with GWO-PSO and PSO.

	Average power	Vibration reduction	Maximum rotation velocity	Maximum force
GWO-PSO	63.08 W	20.22%	876 rad/s	9701 N
PSO	39.68 W	14.79%	624 rad/s	9632 N

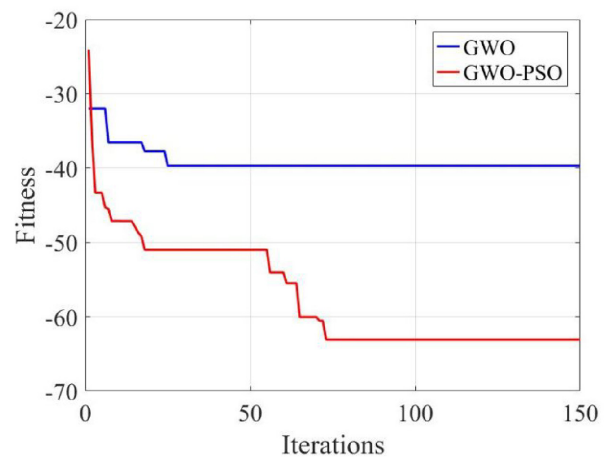


Figure 20. Fitness values calculated by the GWO-PSO and GWO with iterations.

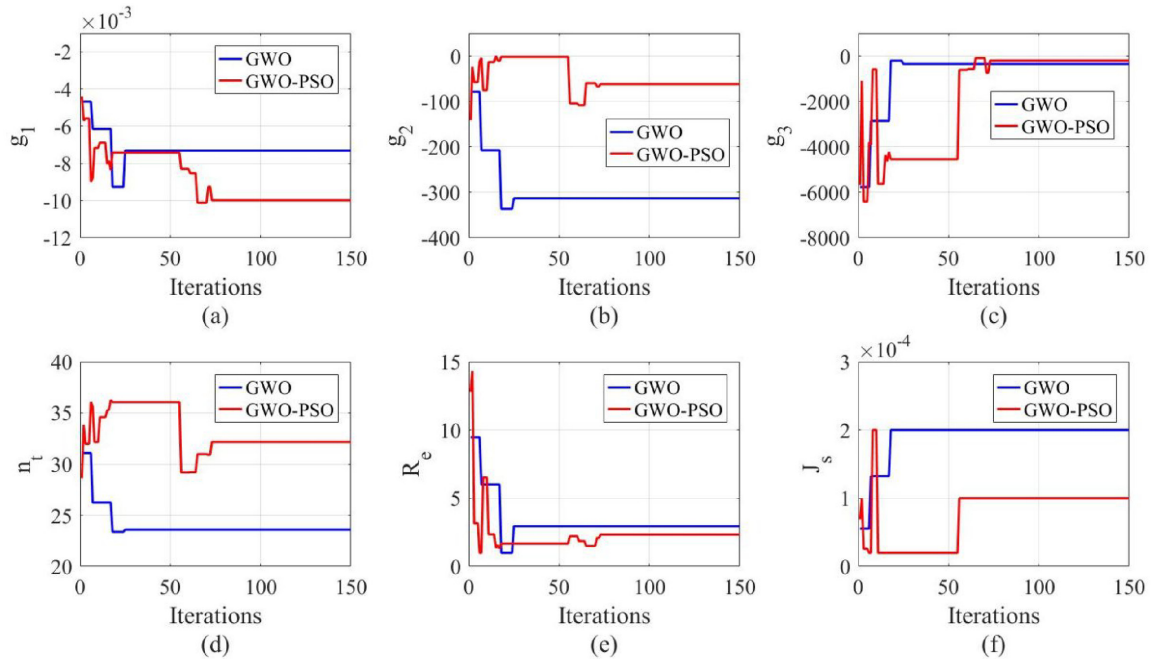


Figure 21. Constraint function values (a) g_1 , (b) g_2 , (c) g_3 , and optimized parameters (d) n_g , (e) R_e , (f) J_s obtained by the GWO-PSO and GWO with iterations.

required resistance value. Hence, the design requirement of the external impedance can be addressed by the FOCV circuit technology.

5.2.2. Instantaneous performance of optimized ERSA under vehicle-ERSA coupling simulation. Based on the vehicle-ERSA coupled model, Figure 22 presents the instantaneous performance of the optimized ERSA. The RMS value of the suspension vibration velocity with the ERSA equipped is 0.0394, achieving a 20.22% decrease compared with the original value of 0.0494. As shown in Figure 22(a) and (b), the maximum values of the generator rotation velocity and ERSA force are 876 rad/s and 9701 N, respectively, lower than their bounds. The average power of 63 W can meet the design demand of 30 W, and the spare part can be stored in batteries and then supplied in the case of insufficient power generation. Table 5 compares two ERSAs designed with GWO-PSO and PSO respectively. The GWO-PSO fully utilizes the boundary condition of generator rotational velocity, as a result, the designed ERSA exhibits a better average power and vibration reduction effect compared to the one designed with PSO. The next stage is to manufacture an ERSA prototype with optimized parameters, install the optimized ERSA on the secondary suspension, and evaluate its performance in field tests.

6. Conclusions

In this paper, a railway vehicle-track coupled model is established by considering the interaction force with the

ERSA. Based on this model, a parameter sensibility analysis concerning the vibration energy harvesting performance and a potential assessment study are conducted, along with a novel systematic design approach proposed for ERSA. Regarding the work in this paper, key conclusions can be drawn as below:

- (1) In the parameter sensibility analysis, the effects of the ERSA, vehicle, and environmental parameters on the energy harvesting performance are investigated. It is found that operation speed, vehicle load, and track irregularity are the three main factors that affect the generated power. It indicates that high speed, heavy load, and rough track conditions, originally magnifying the operation risk of wagons, have now become favorable from the power generation perspective. In addition, uphill and downhill will slightly increase power generation. However, a sharp curve will reduce the power generation capacity to some extent.
- (2) Energy harvesting potential assessment is conducted on American, German, and Chinese track spectrums and several field-measured freight lines. The performance of a freight wagon with 90 t load at 90 km/h can produce an average power ranging from 33 to 960 W per absorber. The power performance on the field-measured track spectrums of the Daqin and Shuohuang lines is between FRA class 5 and class 6. The significance of this analysis is

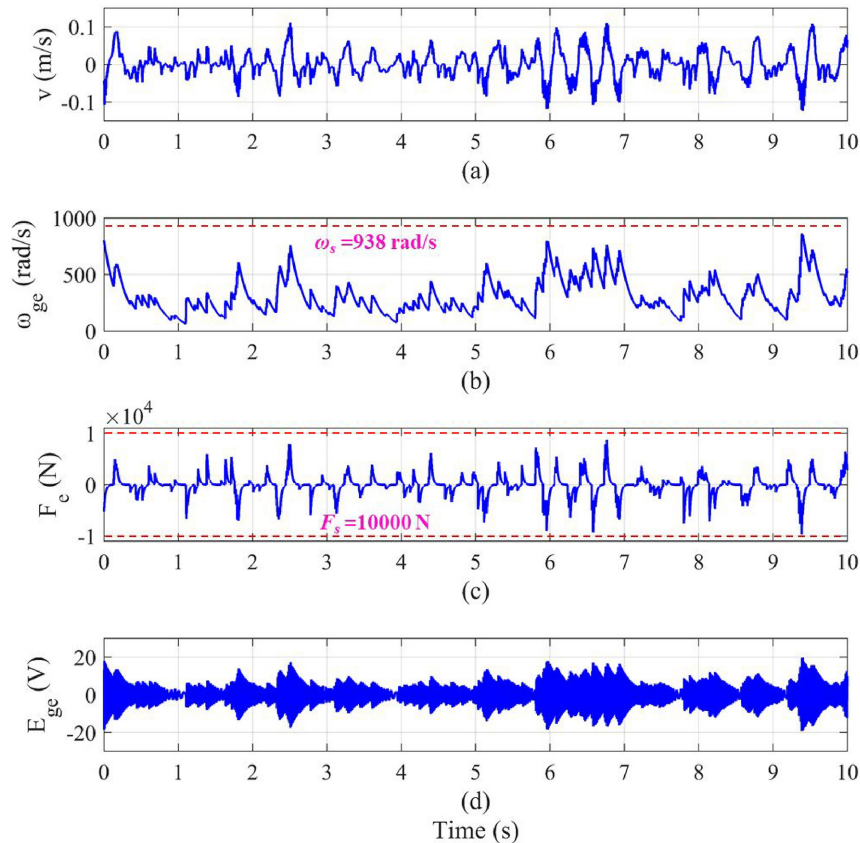


Figure 22. Simulation results of the optimized ERSA under vehicle-ERSA coupling: (a) the suspension vibration velocity, (b) the generator rotation velocity, (c) the ERSA force, and (d) the generated phase voltage of ERSA.

to predict whether the power performance on the current freight line meets the requirements of the electrical devices served to avoid invalid design.

- (3) Taking a type of MMR-based ERSA as the optimization object, its digital twin is established considering the engagement and disengagement modes of one-way clutches, which is validated to be effective with a difference ranging from 2.54 to 4.54%, 8.25 to 15.78%, and -4.28 to 8.12% regarding the RMS values of the generator velocity, ERSA force, and ERSA voltage compared to test results.
- (4) The novel systematic design approach based on the hybrid GWO-PSO algorithm and the vehicle-ERSA coupled model is proposed for solving the constrained optimization problem in designing ERSA. The GWO-PSO exhibits a stronger exploration capacity than the conventional GWO in avoiding being trapped in a local optimum. The optimized ERSA produces an average power of 63 W under stochastic suspension vibration and 20.22% shock absorption on secondary suspension. The maximum generator rotation velocity and maximum

ERSA force are lower than the bounds, guaranteeing the reliability and service life of the ERSA pivotal components.

Declaration of conflicting interests

The authors declared no potential conflicts of interest with respect to the research, authorship, and/or publication of this article.


Funding

The authors disclosed receipt of the following financial support for the research, authorship, and/or publication of this article: This work was mainly carried out by the first author during his visit to Nanyang Technological University, and sponsored by the China Scholarship Council (Grant No. 202206260157). The partial tests were supported by the National Natural Science Foundation of China (Grant No. 51728503) and the Shanghai Collaborative Innovation Research Center for Multi-network & Multi-model Rail Transit.

Data availability statement

The data that support the findings of this study are available upon reasonable request from the authors.

ORCID iD

Liwei Dong  <https://orcid.org/0000-0003-3675-0674>

References

- Abdelkareem MAA, Xu L, Ali MKA, et al. (2019) Analysis of the prospective vibrational energy harvesting of heavy-duty truck suspensions: A simulation approach. *Energy* 173: 332–351.
- Aboelmaaref MM, Zayed ME, Elsheikh AH, et al. (2021) Design and performance analysis of a thermoelectric air-conditioning system driven by solar photovoltaic panels. *Proceedings of the Institution of Mechanical Engineers Part C Journal of Mechanical Engineering Science* 235(20): 5146–5159.
- Bakhtiyari Yekta H and Fakhari V (2023) A novel optimized design of an energy harvester using magnetoelectric transducers. *Journal of Intelligent Material Systems and Structures* 34: 2061–2073.
- Dong L, Hu G, Yu J, et al. (2023) Maximizing onboard power generation of large-scale railway vibration energy harvesters with intricate vehicle-harvester-circuit coupling relationships. *Applied Energy* 347: 121388.
- Dash RC, Sharma N, Maiti DK, et al. (2022) Uncertainty analysis of galloping based piezoelectric energy harvester system using polynomial neural network. *Journal of Intelligent Material Systems and Structures* 33(16): 2019–2032.
- Delattre G, Vigne S, Brenes A, et al. (2023) A new approach to design electromagnetic transducers for wideband electrically-tuned vibration energy harvesting. *Journal of Intelligent Material Systems and Structures* 34(11): 1314–1329.
- Dong L, Yang F, He A, et al. (2022) Investigation on energy-regenerative shock absorber with adjustable damping and power for freight wagons. *Energy Conversion and Management* 254: 115228.
- Du Y, Tang Q, He W, et al. (2021) Harvesting ambient mechanical energy by multiple mode triboelectric nanogenerator with charge excitation for self-powered freight train monitoring. *Nano Energy* 90: 106543.
- Dziadok B, Kucharek M and Starzyński J (2022) Powering the WSN node for monitoring rail car parameters, using a piezoelectric energy harvester. *Energies* 15(5): 1641.
- Fang Z, Tan X, Liu G, et al. (2022) A novel vibration energy harvesting system integrated with an inertial pendulum for zero-energy sensor applications in freight trains. *Applied Energy* 318: 119197.
- Gao M, Cong J, Xiao J, et al. (2020) Dynamic modeling and experimental investigation of self-powered sensor nodes for freight rail transport. *Applied Energy* 257: 113969.
- Gao M, Wang P, Wang Y, et al. (2018) Self-powered ZigBee wireless sensor nodes for railway condition monitoring. *IEEE Transactions on Intelligent Transportation Systems* 19(3): 900–909.
- Hao X, Yang J, Yang F, et al. (2023) Analysis and expression of track irregularity spectrum of heavy-haul railway. *Journal of the China Railway Society* 45: 115–125.
- Hegendörfer A, Steinmann P and Mergheim J (2023) An implicitly coupled finite element-electronic circuit simulator method for efficient system simulations of piezoelectric energy harvesters. *Journal of Intelligent Material Systems and Structures* 34: 1825–1840.
- Hu G, Zhao C, Yang Y, et al. (2022) Triboelectric energy harvesting using an origami-inspired structure. *Applied Energy* 306: 118037.
- Jerrelind J, Allen P, Gruber P, et al. (2021) Contributions of vehicle dynamics to the energy efficient operation of road and rail vehicles. *Vehicle System Dynamics* 59(7): 1114–1147.
- Jin L, Deng W, Su Y, et al. (2017) Self-powered wireless smart sensor based on maglev porous nanogenerator for train monitoring system. *Nano Energy* 38: 185–192.
- Jin T, Sun Z, Li L, et al. (2020) Triboelectric nanogenerator sensors for soft robotics aiming at digital twin applications. *Nature Communications* 11(1): 5381.
- Kuang Y, Chew ZJ, Ruan T, et al. (2021) Magnetic field energy harvesting from the traction return current in rail tracks. *Applied Energy* 292: 116911.
- Li L, Wang W, Luo D, et al. (2021) A high-efficiency energy regeneration shock absorber based on twin slider-crank mechanisms for self-powered sensors in railway cars. *Smart Materials and Structures* 30(1): 015014.
- Lin T, Wang JJ and Zuo L (2018) Efficient electromagnetic energy harvester for railroad transportation. *Mechatronics* 53: 277–286.
- Li Z, Zuo L, Kuang J, et al. (2013) Energy-harvesting shock absorber with a mechanical motion rectifier. *Smart Materials and Structures* 22(2): 025008.
- Maravandi A and Moallem M (2015) Regenerative shock absorber using a Two-Leg motion conversion mechanism. *IEEE/ASME Transactions on Mechatronics* 20(6): 2853–2861.
- Mi J, Li Q, Liu M, et al. (2020) Design, modelling, and testing of a vibration energy harvester using a novel half-wave mechanical rectification. *Applied Energy* 279: 115726.
- Mirjalili S, Mirjalili SM and Lewis A (2014) Grey Wolf Optimizer. *Advances in Engineering Software* 69: 46–61.
- Pan Y, Lin T, Qian F, et al. (2019) Modeling and field-test of a compact electromagnetic energy harvester for railroad transportation. *Applied Energy* 247: 309–321.
- Qin W, Liu Q, Wang Y, et al. (2023) Increase output of vibration energy harvester by a different piezoelectric mode and branch structure design. *Journal of Physics D: Applied Physics* 56(3): 034001.
- Shaheen MAM, Hasanien HM and Alkuhayli A (2021) A novel hybrid GWO-PSO optimization technique for optimal reactive power dispatch problem solution. *Ain Shams Engineering Journal* 12(1): 621–630.
- Wang R, Allen P, Song Y, et al. (2022) Modelling and analysis of power-regenerating potential for high-speed train suspensions. *Sustainability* 14(5): 2542.
- Wang Z, Zhang T, Zhang Z, et al. (2020) A high-efficiency regenerative shock absorber considering twin ball screws transmissions for application in range-extended electric vehicles. *Energy and Built Environment* 1(1): 36–49.
- Wu X, Qi L, Zhang T, et al. (2021) A novel kinetic energy harvester using vibration rectification mechanism for self-powered applications in railway. *Energy Conversion and Management* 228: 113720.
- Zhai W (2015) *Vehicle-Track Coupled Dynamics*. Singapore: Springer.
- Zhang Y, Guo K, Wang D, et al. (2017) Energy conversion mechanism and regenerative potential of vehicle suspensions. *Energy* 119: 961–970.

A. Appendix A

A.1 Grey wolf optimization algorithm

A.1.1 Social hierarchy. The grey wolf optimization (GWO) algorithm was first proposed by Mirjalili et al. (2014). The principle of the GWO is inspired by the strict social hierarchy and hunting strategy of grey wolves in the natural world. In a wolf group, wolves are divided into four categories: alpha, beta, delta, and omega. Alpha is the leader of the group, responsible for controlling the entire wolf group. All other categories of wolves need to obey the orders of wolves at a high priority level.

In the corresponding mathematical representation, the alpha α is considered the fittest solution, followed by the beta β and delta δ . The omega ω is the rest of the candidate solutions, following the three categories of wolves.

A.1.2 Encirclement behavior. The encirclement behavior of gray wolves during hunting can be mathematically modeled as

$$\vec{D} = \left| \vec{C} \cdot \vec{X}_p - \vec{X}(t) \right| \quad (\text{A1})$$

$$\vec{X}(t+1) = \vec{X}_p - \vec{A} \cdot \vec{D} \quad (\text{A2})$$

where \vec{A} and \vec{C} represent the coefficient vectors; \vec{X}_p and $\vec{X}(t)$ are the positions of the prey and wolf, respectively; t is the number of iterations.

The coefficient vectors \vec{A} and \vec{C} can be obtained as

$$\vec{A} = 2\vec{a} \cdot \vec{r}_1 - \vec{a} \quad (\text{A3})$$

$$\vec{C} = 2 \cdot \vec{r}_2 \quad (\text{A4})$$

where the elements in \vec{a} linearly decrease from 2 to 0 in the iterative process; \vec{r}_1 and \vec{r}_2 are random vectors between [0, 1].

A.1.3 Hunting mechanism. α , β , and δ with better fitness imply they have more experience identifying potential prey locations. They usually play a leading role in the hunting process, and other search agents need to update their positions according to the first three best solutions obtained, which can be presented as

$$\begin{cases} \vec{D}_\alpha = \left| \vec{C}_1 \cdot \vec{X}_\alpha - \vec{X} \right| \\ \vec{D}_\beta = \left| \vec{C}_2 \cdot \vec{X}_\beta - \vec{X} \right| \\ \vec{D}_\delta = \left| \vec{C}_3 \cdot \vec{X}_\delta - \vec{X} \right| \end{cases} \quad (\text{A5})$$

$$\begin{cases} \vec{X}_1 = \vec{X}_\alpha - \vec{A}_1 \cdot (\vec{D}_\alpha) \\ \vec{X}_2 = \vec{X}_\beta - \vec{A}_2 \cdot (\vec{D}_\beta) \\ \vec{X}_3 = \vec{X}_\delta - \vec{A}_3 \cdot (\vec{D}_\delta) \end{cases} \quad (\text{A6})$$

$$\vec{X}(t+1) = \frac{\vec{X}_1 + \vec{X}_2 + \vec{X}_3}{3} \quad (\text{A7})$$

A.1.4 Exploring and attacking behaviors. \vec{A} is a random vector ranging from $-2\vec{a}$ to $2\vec{a}$ where a linearly declines from 2 to 0 with iterations. When the value of \vec{A} is between [-1, 1], the next position of the search agent can be anywhere between the current position and the position of prey. If $|\vec{A}| < 1$, the wolves are forced to attack the prey. They represent two behaviors: searching for the prey and attacking the prey in hunting. However, the GWO needs to enhance its exploration ability with more operators to avoid being trapped in a local solution.

A.2 Particle swarm optimization algorithm

The particle swarm optimization (PSO) algorithm is a classical metaheuristic optimizer that solves optimization problems by simulating the behavior of groups such as birds and fish. In the PSO, each solution is considered as a particle, and its suitability is determined by an objective function. The particles are generated in a multidimensional search space. Then, they gradually move towards more promising solution areas with the experience of their own and neighboring particles, finally finding the optimal solution. The PSO has been widely exploited for different optimization problems due to the advantages of fewer parameters to adjust and easy-to-implement. The velocity and the position of each particle are updated according to the following rules:

$$v_i(t+1) = w \cdot v_i(t) + C_1 \cdot rand_1 \cdot (Pbest_i - x_i) + C_2 \cdot rand_1 \cdot (Gbest_i - x_i) \quad (\text{A7})$$

$$x_i(t+1) = x_i(t) + v_i(t+1) \quad (\text{A9})$$

where $v_i(t)$ and $x_i(t)$ represent the velocity and position of the i th particle; C_1 and C_2 are the personal and global learning coefficients within the range of [0, 2]; w is the inertia factor determining the local search ability; $Pbest_i$ and $Gbest_i$ are the best positions of the i th particle and the whole swarm ever arrived.